

# Ultrafast electron-phonon scattering in antiferromagnetic Dirac semimetals

Marius Weber,<sup>1</sup> Kai Leckron,<sup>1</sup> Libor Šmejkal,<sup>2</sup> Jairo Sinova,<sup>2</sup> Baerbel Rethfeld,<sup>1</sup> and Hans Christian Schneider<sup>1</sup>

<sup>1</sup>*Department of Physics and Research Center OPTIMAS,  
University of Kaiserslautern-Landau, 67663 Kaiserslautern, Germany*

<sup>2</sup>*Institut für Physik, Johannes Gutenberg University Mainz, 55099 Mainz, Germany*

(Dated: November 7, 2023)

Topological antiferromagnetic systems, which exhibit anisotropic band structures combined with complex relativistic spin structures in momentum space, have shown strong magnetoresistance effects driven by Dirac fermion characteristics. While these new antiferromagnets have been studied in transport experiments, very little is known about their spin-dependent electronic dynamics on ultrafast timescales and far-from-equilibrium behavior. This paper investigates theoretically the spin-dependent electronic dynamics due to electron-phonon scattering in a model electronic band structure that corresponds to a Dirac semimetal antiferromagnet. Following a spin conserving instantaneous excitation we obtain a change of the antiferromagnetic spin polarization due to the scattering dynamics for the site-resolved spin expectation values. This allows us to identify fingerprints of the anisotropic band structure in the carrier dynamics on ultrashort timescales which should be observable in present experimental set-ups.

## I. INTRODUCTION

The field of antiferromagnetism has seen a surge in interest over the last years due to its potential for applications in current-based spintronics [1–5]. One particularly appealing property of the AFM phase is its robustness against magnetic perturbations. Further, the characteristics of magnonic excitations in antiferromagnets are very different from ferromagnets and their resonance frequencies make it possible to address them directly by THz fields. However, their insensitivity to magnetic fields also leads to a big challenge, as it is more difficult to excite and measure their order parameter, i.e., the Néel vector. This sets them apart from ferromagnetic materials, where the magnetization may be manipulated relatively easily by external fields, but which suffer, among other things, from stray fields and thermal stability.

Only recently, there have been attempts to study

the excitation of AFMs by optical fields on ultrashort timescales [6, 7]. While the coupling of the spin-dependent electronic dynamics to the AFM order parameter is currently being investigated [8], it is also of interest to understand the dynamics of carriers, which are photoexcited to states above the Fermi energy where the microscopic details of electronic scattering processes might be important.

This paper presents a theoretical study of the spin-dependent electronic dynamics in an AFM model system due to incoherent scattering processes using a microscopic approach. We employ the minimal AFM model recently proposed by Šmejkal et al. [9]. It consists of two doubly degenerate bands and exhibits a band structure with pronounced anisotropies including two Dirac-points. For this system, we compute the microscopic electron-phonon scattering dynamics, which leads, in conjunction with spin-orbit coupling in the electronic states, to spin flip/spin relaxation processes. This type of spin-dependent dynamics of electrons in degenerate bands originating from a scattering mechanism that by itself is spin-independent (or very weakly spin dependent) is the Elliott-Yafet mechanism. While the Elliott-Yafet mechanism was originally proposed for electron-spin resonance [10], *dynamical* calculations of momentum resolved occupation numbers [11–15] can also describe far from equilibrium effects as they arise after optical excitation with ultrashort pulses. However, such microscopic momentum resolved calculations are numerically demanding so that calculations have often been limited to simplified band structures consisting of only a few bands and/or using isotropic band structures [16, 17]. Effects due to the anisotropic character of the band structure may be captured, for instance, by limiting the  $\mathbf{k}$ -space to an irreducible wedge and a low number of  $\mathbf{k}$ -points [12], or projecting energy-dependent occupation numbers back to momenta through a band structure mapping [18, 19]. Our first goal is to explore electronic excitations in the spin and energy “landscape” presented by topological an-

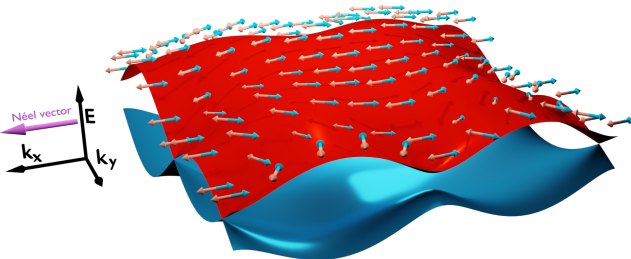


FIG. 1. Band structure of the minimal model of an antiferromagnetic Dirac-semimetal. The arrows on top of the upper two degenerate bands (red surface) represent the  $k$ -local spin expectation values for each band, blue arrows correspond to the upper ‘-’-band and red arrows to the upper ‘+’-band described in the main text.

tiferromagnets as introduced in [20] with a dynamical approach that is free from the above-mentioned restrictions. This allows us to determine the consequences of incoherent electron-phonon scattering in the full Brillouin-zone of the AFM without approximations that result from placing symmetry or isotropy restrictions on the dynamical distribution functions.

We stress that the anisotropic spin structure has two facets in antiferromagnets: First, in any Kramers degenerate band structure one has opposite expectation values of the (vector) spin in the degenerate Bloch states at each  $\mathbf{k}$ . Second, the antiferromagnetic order is reflected in the different spins in the magnetic unit cell, for instance in an A-B structure in real space, as in the present model. Investigating the dynamics of both spin structures on ultrafast timescales is a central goal of this paper.

This paper is organized as follows. In Sec. 2 we present the model band structure and discuss our parameters and the resulting spin texture. Further, we introduce the equation of motion for the electronic distribution function due to electron-phonon scattering. In Sec. 3 we present the calculated spin-dependent electron dynamics after an instantaneous excitation process. We discuss the fingerprints of the band structure in the electronic dynamics and the consequences of the electronic scattering process for the antiferromagnetic spin polarization. We present our conclusions in Sec. 4.

## II. THEORY

As motivated above, we consider the following minimal antiferromagnetic model as introduced in Refs. [9, 20], which is defined for a two-dimensional  $\mathbf{k} = (k_x, k_y)$ -space by the effective Hamiltonian

$$H(\mathbf{k}) = A(\mathbf{k})\tau_x \otimes \mathbb{1} + \alpha(\mathbf{k})\tau_z \otimes \sigma_x + \beta(\mathbf{k})\tau_z \otimes \sigma_y + J_z\tau_z \otimes \sigma_z, \quad (1)$$

with momentum-dependent coefficients  $A(\mathbf{k}) = -2t \cos(\frac{k_x}{2}) \cos(\frac{k_y}{2})$ ,  $\alpha(\mathbf{k}) = J_x - \lambda \sin(k_y)$ , and  $\beta(\mathbf{k}) = J_y + \lambda \sin(k_x)$ . The coefficient  $A$  is a nearest-neighbor hopping term that couples the orbital degrees of freedom, whereas  $\alpha$  and  $\beta$  contain the spin-orbit coupling  $\lambda$  and the Cartesian components  $J_\chi = J_n(\mathbf{n} \cdot \mathbf{e}_\chi)$  of the antiferromagnetic vector  $\mathbf{J} = J_n\mathbf{n}$  for a fixed direction of the Néel vector  $\mathbf{n}$ . The Hamiltonian (1) acts on a 4-dimensional space of electronic states with two degrees of freedom due to orbitals at the A and B sites and two spin degrees of freedom. The  $\sigma_\chi$  and  $\tau_\chi$  are Pauli matrices acting separately on the two spin and orbital degrees of freedom.

The eigenstates of Hamiltonian (1) are doubly degenerate with eigenenergies

$$E(\mathbf{k}) = \pm \sqrt{A(\mathbf{k})^2 + \alpha(\mathbf{k})^2 + \beta(\mathbf{k})^2 + J_z^2}, \quad (2)$$

which depend on  $\mathbf{k}$  through  $A(\mathbf{k})$ ,  $\alpha(\mathbf{k})$  and  $\beta(\mathbf{k})$ . Following the procedure of Refs. [21, 22], we fix the eigenstates in the two degenerate subspaces by choosing them such that they diagonalize the spin operator in the direction of the Néel-vector at each  $\mathbf{k}$ -point. More precisely, labeling the eigenstates at  $\mathbf{k}$  with band index  $\nu$ , we have  $\langle \mathbf{k}\nu | (\mathbf{n} \cdot \boldsymbol{\sigma}) | \mathbf{k}\nu' \rangle = 0$  for  $\nu \neq \nu'$ . Here  $\boldsymbol{\sigma}$  denotes the vector of Pauli matrices, which only acts on the spin degree of freedom.

The band structure (2) is shown in Fig. 1. We use a lattice constant of  $a = 0.45331$  nm which leads to a Brillouin zone with  $k_{\max} = 6.82$  nm $^{-1}$ , and we set  $t = 100$  meV,  $\lambda = 1.5 \times t$  and  $J_n = 0.6 \times t$ . The model exhibits two *Dirac points* located at the border of the Brillouin zone at  $\mathbf{k}_1 = (k_{\max}, 0.9$  nm $^{-1})$  and  $\mathbf{k}_2 = (k_{\max}, 6.0$  nm $^{-1})$ . Only at these two points the upper and lower bands touch and the dispersion is approximately linear. Our choice of the parameter  $t$ , which has been reduced compared to Ref. [20], makes the characteristic band structure feature less steep. The spin expectation values are defined by  $\langle \boldsymbol{\sigma} \rangle_{\mathbf{k}\nu} = \langle \mathbf{k}\nu | \boldsymbol{\sigma} | \mathbf{k}\nu \rangle$  and shown for the upper band as arrows on top of the band structure in Fig. 1. At each  $\mathbf{k}$ , the spin expectation value of one of the degenerate bands is aligned anti-parallel to that of the other one. The whole band structure shows a non-trivial spin texture. For definiteness, we label the four bands as: “upper”/“lower” identifying the two sets of degenerate bands, and ‘+’/‘-’ according to the dominant spin character in each degenerate subspace. The label ‘+’ indicates a spin direction that mostly points in the direction of the Néel vector and should not be confused with the sign of the eigenenergy (2). It should also be pointed out that the spin direction close to the border of the Brillouin zone may point in a different direction from the one used as the label.

For the incoherent electronic scattering transitions after ultrafast optical excitation, there is usually a much larger phase space available than for transport/dynamics close to the Fermi energy. The optically excited electrons sample the spin structure of the sequence of final states available to them. In order to describe these dynamics in the present paper, we consider electron scattering with longitudinal acoustic phonons. This scattering process can relax both carrier energy and momentum, and has been shown to play an important role on ultrafast timescales in ferromagnets [12, 13, 15, 17, 23, 24]. The fundamental dynamical quantities are the electronic distributions  $n_{\mathbf{k}}^\nu = \langle c_{\mathbf{k},\nu}^\dagger c_{\mathbf{k},\nu} \rangle$ , i.e., the diagonal elements of the single-particle density matrix defined in terms of creation and annihilation operators  $c_{\mathbf{k},\nu}^{(\dagger)}$  for electrons in the state  $|\mathbf{k}, \nu\rangle$  with crystal momentum  $\hbar\mathbf{k}$  and band index  $\nu$ .

The equation of motion (EOM) for the electronic distributions due to the interaction with phonons is used in the form

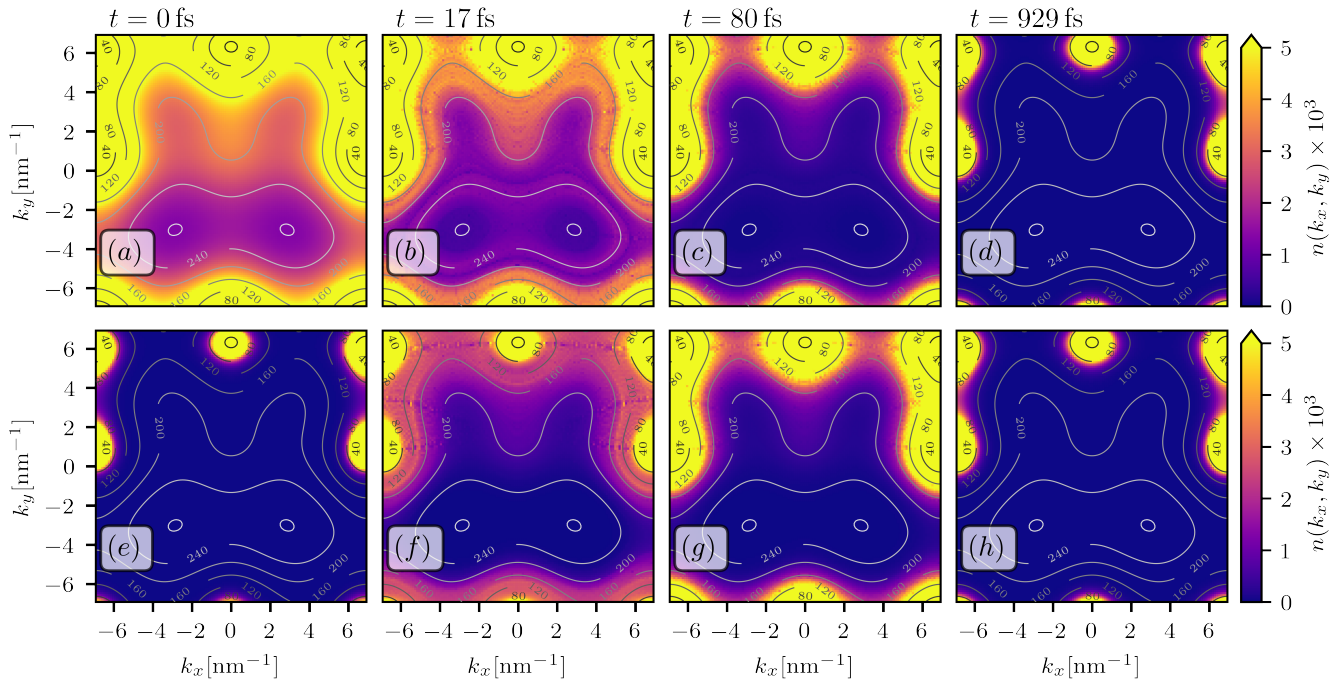


FIG. 2. Color map of electron distributions  $n_{\nu, \mathbf{k}}$  vs.  $\mathbf{k}$  for the upper degenerate bands ('+' band top row, '-' band bottom row) with a contour plot of the band structure as overlay. Contours and corresponding energy labels range from bright (280 meV) to dark lines (40 meV). Distributions are shown directly after the instantaneous excitation in the upper bands (a)&(e), shortly after excitation (b)&(f), when the upper bands are close to a quasiequilibrium (c)&(g), and after relaxation within the upper bands (d)&(h).

$$\frac{\partial}{\partial t} n_{\mathbf{k}}^{\nu} = \frac{2\pi}{\hbar} \sum_{\mathbf{k}'\nu'} |g_{\mathbf{k}'\nu', \mathbf{k}\nu}|^2 \left[ ((1 + N_{\mathbf{k}'-\mathbf{k}})(1 - n_{\mathbf{k}'}^{\nu'})n_{\mathbf{k}}^{\nu'} - N_{\mathbf{k}'-\mathbf{k}}(1 - n_{\mathbf{k}'}^{\nu'})n_{\mathbf{k}}^{\nu})\delta(\Delta E_{-}^{\nu'\nu}) \right. \\ \left. - ((1 + N_{\mathbf{k}-\mathbf{k}'})(1 - n_{\mathbf{k}'}^{\nu'})n_{\mathbf{k}}^{\nu} - N_{\mathbf{k}-\mathbf{k}'}(1 - n_{\mathbf{k}'}^{\nu'})n_{\mathbf{k}}^{\nu'})\delta(\Delta E_{+}^{\nu'\nu}) \right], \quad (3)$$

where  $\Delta E_{\pm}$  is a shorthand notation for the energy differences  $\Delta E_{\pm} = \varepsilon_{\mathbf{k}}^{\nu} - \varepsilon_{\mathbf{k}'}^{\nu'} \pm \hbar\omega_q$  that arise from energy conservation for the electron-phonon scattering process involving a phonon energy of  $\hbar\omega_q$ , where the phonon momentum is  $q = |\mathbf{k}_1 - \mathbf{k}|$ . The phonons are assumed to form a bath so that their occupation numbers are always given by a Bose-Einstein distribution  $n_B(\hbar\omega_q)$  with an equilibrium temperature of  $T^{(\text{eq})} = 150$  K. We compute the numerical solution of EOM (3) in the complete Brillouin zone to resolve the *anisotropic* dynamics. For the phonon dispersion we assume a standard form  $\hbar\omega_{\mathbf{q}} = \hbar c_{\text{pn}} |\sin(\frac{a}{2}q)| \frac{2}{a}$  with lattice constant  $a$  and speed of sound  $c_{\text{pn}} = 5$  nm ps $^{-1}$ . For the electron-phonon matrix elements we use the expression

$$g_{\mathbf{k}\nu, \mathbf{k}_1\nu_1} \simeq \sqrt{\frac{\hbar}{2m_{\text{ion}}\omega_q}} Dq \langle \mathbf{k}\nu | \mathbf{k}_1\nu_1 \rangle, \quad (4)$$

with a deformation potential,  $D = 3$  eV [23]. The overlap  $\langle \mathbf{k}\nu | \mathbf{k}_1\nu_1 \rangle$  includes the dependence on the relative orien-

tation of initial and final momenta of intra- and interband transitions.

### III. RESULTS AND DISCUSSION

In order to study characteristics of spin dependent carrier scattering due to electron-phonon interactions we assume that the excitation process conserves the total ensemble spin expectation value, i.e., integrated over all bands. To this end, we will assume that electrons from the lower '+' band are excited to the upper '+', but that the memory of the detailed optical excitation process has been lost due to elastic electron-electron scattering and dephasing processes. We will thus approximate the excitation process as instantaneous and assume that it leads to the distributions shown for the upper '+' and '-' bands in Fig. 2 (a) and (e), respectively: a cold ( $T^{(\text{eq})} = 150$  K) Fermi-Dirac (FD) distribution in the unexcited '-' bands, see Fig. 2(e), and a

hot ( $T^{\text{ex}} = 1500$  K) FD distribution in the excited ‘+’ bands, see Fig. 2(a). The initial carrier distributions thus depend only on the band energies. Starting from these initial distributions, the inelastic electron-phonon scattering dynamics are computed using Eq. (3). Note that the upper ‘+’-band contains additional electron density due to the excitation, leading to an equal but opposite change in electron density in the lower ‘+’-band, i.e., the creation of ‘holes’. We mainly discuss the dynamics for the upper bands in the following because the lower bands exhibit the same dynamics for holes.

Figure 2 shows snapshots of the electronic distribution functions in the 2D  $k$ -space as they evolve due to electron-phonon scattering. The panels (a)–(d) and (e)–(h) display the electron occupations for the upper ‘+’ and ‘-’ bands, respectively. Figs. 2 (a) and (e) show the initial state, i.e., the hot FD distribution in the ‘+’ band (a) and cold FD in the ‘-’ band (e). In Fig. 2(e) the Dirac-points are visible at the left and right boundaries ( $k_x = \pm k_{\text{max}}$ ) because a small electron occupation in the upper bands can exist around these band crossings at finite temperatures. The region with comparatively high occupation  $> 0.05$  in equilibrium around  $k_x = 0 \text{ nm}^{-1}$  and  $k_y \approx 6 \text{ nm}^{-1}$  is a *local* minimum with a gap of 66 meV between the upper and lower bands.

Figure 2(b) reveals that electrons bunch up in the ‘+’ band, as shown by the distinct belts of transient electron occupations located near the equipotential line around 240 meV and between the equipotential lines for 160 meV and 200 meV that develop on a 10 fs time scale and persist up to roughly 50 fs. Note that this is a striking feature of the dynamics as it occurs in regions of the band structure away from a local band minimum where one would expect an increase in density due to a lack of out-scattering phase space. The underlying process is electronic cooling, in which electrons scatter to lower energies within the ‘+’

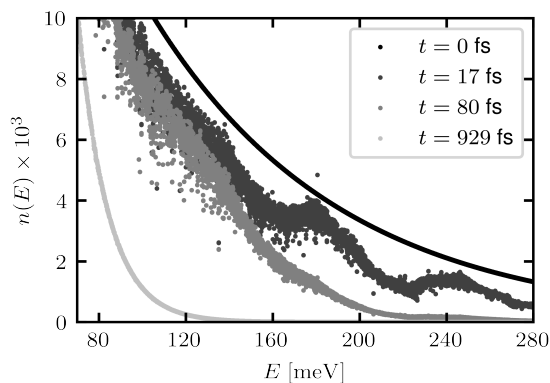


FIG. 3. Electron distributions from the upper ‘+’ band, as shown in Fig. 2 (a)–(d) plotted here vs. energy instead of  $\mathbf{k}$ . The contribution of each  $\mathbf{k}$ -point is shown as a single dot. During the scattering dynamics, electrons bunch up at certain energies and develop a pronounced anisotropy, which shows up here as a spread in the computed  $n(E)$  data.

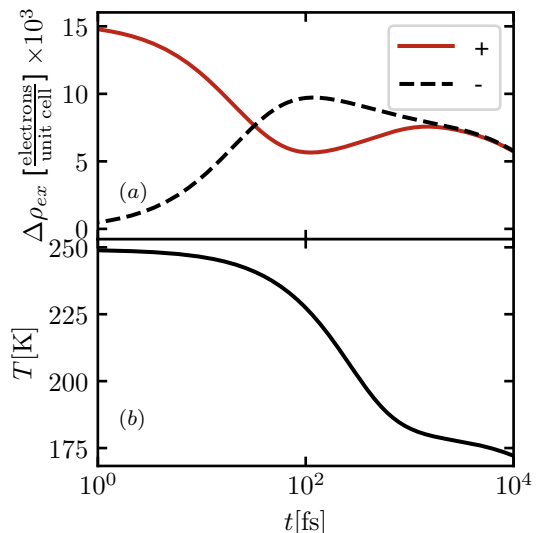


FIG. 4. Electron density in the upper bands (a) and temperature of the whole system (b) over the time.

band, cf. Fig. 2(b), as well as transitions from the ‘+’ to the ‘-’ band due to the finite overlap  $\langle \mathbf{k} + |\mathbf{k}_1 - \rangle$  in the electron-phonon matrix element (4) as shown in Fig. 2(f). In order to exhibit these features more clearly, we plot in Fig. 3 the electronic distributions in the ‘+’-band vs. energy instead of momentum  $\mathbf{k}$  for the same times as in Figs. 2 (a)–(d). Each dot represents the distribution at a  $\mathbf{k}$ -point with the respective energy [25]

Figure 3 demonstrates two characteristics of electronic dynamics in such a band structure: First, the electrons bunch up in regions of  $k$ -space above the band minima, i.e., the Dirac-points and the local minimum at 33 meV. Second, essentially momentum dependent distributions evolve from an initial state which depends only on the electronic energies, as indicated by the spread of the dots for  $t = 17$  fs and  $t = 80$  fs vs. the formation of a smooth curve for  $t = 0$  fs. We have checked that the formation of these regions of transient non-equilibrium electron distributions is *not* a numerical artifact, but a consequence of the available electronic scattering paths in this specific anisotropic band structure in combination with the phonon dispersion.

Returning to Fig. 2 we examine the remaining snapshots. At  $t = 80$  fs, shown as Figs. 2(c) and (g), a pronounced increase of the electron distribution in the upper ‘-’ band and a decrease of the electron distribution in the upper ‘+’ can be observed. For longer times, shown for  $t = 929$  fs in Figs. 2(d) and (h), the phonons continue to cool the distributions, until a quasi-equilibrium is reached; see also the discussion of Fig. 4 below. On a nanosecond time scale (not shown here) the additional electrons in the upper bands recombine with holes in the lower bands, and the whole system relaxes back to a complete equilibrium.

To obtain a qualitative characterization of the complicated  $k$ -dependent scattering dynamics we compute the

carrier density and energy density in the upper bands. Figure 4(a) shows the deviation of the electron density of the upper bands from its equilibrium value,  $\Delta\rho_{ex}^{\nu}(t) = \rho_{ex}^{\nu}(t) - \rho_{eq}^{\nu}$ . In Fig. 4(b) we plot an effective temperature, which we determine by fitting a Fermi-Dirac distribution with one common temperature for the whole system. This temperature is intended as a measure of the energy density of the non-equilibrium distribution functions. The integrated densities and energy densities contain contributions from all excited carriers, and are only weakly influenced by the dynamics at higher energies, which were analyzed in detail in Fig. 3. Our excitation elevates roughly 0.015 electrons per unit cell from the lower '+' to the upper '+' band. This additional density in the excited upper '+'-band decreases as the density in the upper '-'-band increases which is caused by spin-flip scattering between the upper bands. This is essentially the signature of an Elliott-Yafet type spin flip or spin relaxation mechanism in this antiferromagnetic system and is mainly determined by the anisotropic band and spin structure of the single-particle Bloch states. The equilibration between the two upper degenerate bands in Fig. 4(a) is accompanied by a fast decrease of the effective temperature in Fig. 4(b) up to 2 ps, which is a signature of pronounced change of the microscopic electronic distributions due to electron-phonon scattering processes. Afterwards the scattering to the lower bands leads to a slower decrease of the temperature in Fig. 4(b).

So far we have investigated the features of the electronic dynamics in the band structure. We now turn to a characterization of the magnetic properties, for which the whole BZ including the Dirac points plays an important role. The antiferromagnetic spin polarization is a result of the staggered spins at A and B sites. From the dynamical electron distributions, we compute the  $\mathbf{k}$  dependent *ensemble* spin expectation values, for which we also distinguish between contributions from A and B orbitals

$$\begin{aligned} \Delta\langle s_x \rangle_{A/B}(t) &= \sum_{\mathbf{k}, \nu} \langle \sigma_x \otimes P_{A/B} \rangle_{\mathbf{k}\nu} (n_{\mathbf{k}}^{\nu}(t) - n_{\mathbf{k}}^{\nu}(-\infty)) \\ &\equiv \langle s_x \rangle_{A/B}(t) - \langle s_x \rangle_{A/B}^{eq}. \end{aligned} \quad (5)$$

Here we used the projectors  $P_{A/B}$  on orbitals at sites A and B, respectively. The top part of Fig. 5(a) shows the spin orientation of the *single-particle* spin  $\langle \sigma \rangle_{\mathbf{k}\nu}$  for the upper '+' band in the whole BZ. The remaining two graphs in Fig. 5(a) illustrate the contributions from sites A and B, respectively. The A/B character of the band states changes along the lines connecting the Dirac points in the Brillouin zone.

Figure 5(b) connects the information contained in Fig. 5(a) with the band structure for the  $k$  space region around the Dirac point. Along the high symmetry lines  $M' \rightarrow X \rightarrow M$  the dispersion of the upper and lower bands are shown together with the site projected spin expectation values and the corresponding orbital character for the '+' bands. Figure 5 already indicates that

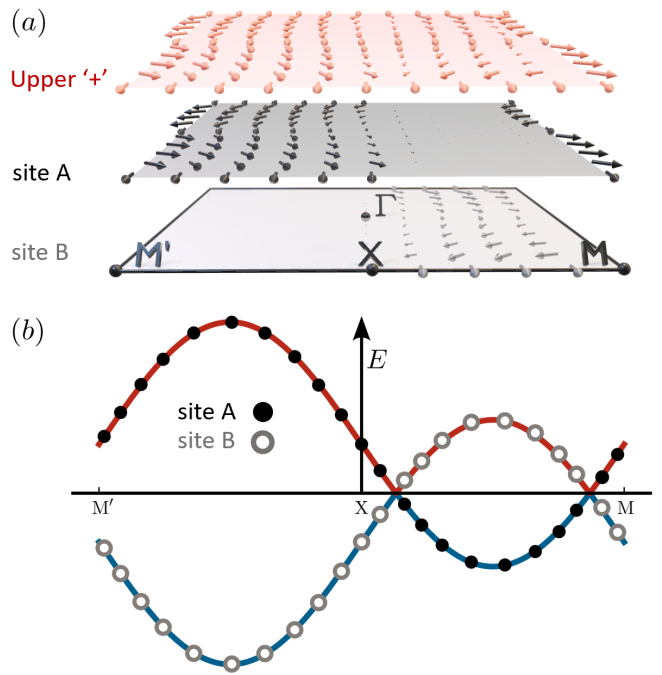


FIG. 5. (a) Spin expectation values  $\langle \sigma \rangle_{\mathbf{k}\nu}$  of the Bloch states for the upper '+'-band (red arrows), contributions from orbitals at site A (black arrows) and orbitals at site B (gray arrows). The Brillouin zone including relevant high symmetry points is shown as a square for site B. (b) Band structure and corresponding site-resolved spins along the high-symmetry line  $M' \rightarrow X \rightarrow M$  for upper '+' band (red curve) and lower '+' band (blue curve). The black and gray dots correspond to the spin expectation value pointing out of the plane for contributions from site A and site B, respectively.

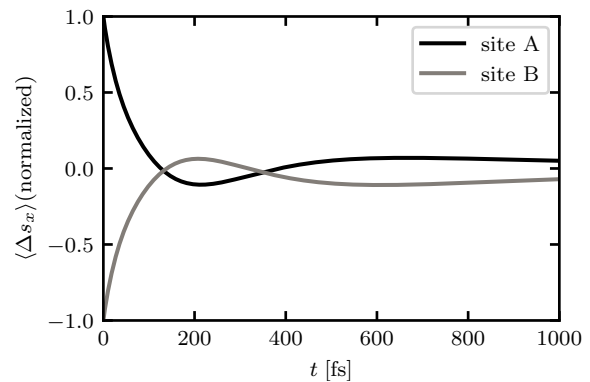


FIG. 6. Change of ensemble spin expectation value in  $x$  direction, projected on site A (black line) and site B (gray line), respectively.  $\langle \Delta s_x \rangle_{A/B}(t)$  has been normalized to its  $t = 0$  value.

the *site-resolved* spin expectation value is changed when electrons from the lower '+' band are elevated to the upper '+' band by an excitation process that conserves the total spin. Such an excitation reduces the spin expecta-

tion value corresponding to site B and increases the one corresponding to site A. This is a consequence of the non-trivial contributions of site A and site B to the bands in the antiferromagnetic Dirac structure visible in Fig. 5(a).

Figure 6 plots the time evolution of the deviation of the site-resolved spin expectation value in the direction of the Néel vector ( $x$ ), as defined in Eq. (5), normalized to its value at  $t = 0$ . The dynamics of the site-resolved spin expectation values occur in opposite directions for A and B sites, so that there is an antiferromagnetic alignment at all times. The normalized  $\langle \Delta s_x \rangle_A$ , i.e., spin-change contribution from site A, goes through a dip at 200 fs, after which it increases again up to 700 fs. The relaxation back to the equilibrium value of 0 on the nanosecond time scale is associated with the *interband* equilibration. The change of the site-resolved spin occurs while the electron-phonon scattering redistributes electrons between the two upper bands, cf. Fig. 2.

We have normalized the site-resolved spin expectation value to its  $t = 0$  value in order to highlight the dynamics on the scale of the excitation. Normalizing to the equilibrium value  $\langle s_x \rangle_{A/B}^{\text{eq}}$  would completely obscure this effect as  $\langle s_x \rangle_{A/B}^{\text{eq}}$  is on the order of the carrier density, i.e., 2 electrons per unit cell, whereas the excited carrier density for our model excitation for the ‘+’-bands is approximately 0.015 electrons per unit cell. The antiferromagnetic dynamics on ultrashort timescales as shown in Fig. 6 have been obtained from the microscopic distribution functions, as one can also do for an itinerant ferromagnet [15]. In contrast, in an itinerant ferromagnet with spin-split bands, the ferromagnetic polarization would be directly related to the band resolved carrier dynamics, i.e., determination of the carrier distributions in the band structure after excitation suffices to recon-

struct the spin-dependent dynamics, which is clearly not the case for the antiferromagnet if one compares Fig. 6 to Fig. 4(a). Here, only the full microscopic 2D-calculation relates the antiferromagnetic spin character of the dynamics to the charge dynamics, which should be observable in present experimental set-ups.

#### IV. CONCLUSION AND OUTLOOK

We have computed the electronic dynamics in an antiferromagnetic model system due to electron-phonon scattering after an instantaneous spin conserving excitation. The microscopic equations of motion for electron-phonon scattering were solved in the whole Brillouin zone including the pronounced anisotropy in the energy and spin structure that occurs in a Dirac semimetal antiferromagnet. As a result of its unique non-trivial band structure, transient anisotropic electron distributions can develop. We connected the antiferromagnetic spin dynamics via site-projected quantities with the electronic scattering dynamics on ultrashort timescales. From the point of view of ultrafast magnetization dynamics, the results presented here establish a description of antiferromagnetic spin dynamics that is the counterpart to the ferromagnetic magnetization dynamics due to electron-phonon scattering in a fixed band structure [12]. Our results indicate that the computed spin dynamics should be observable using present-day experimental set-ups.

#### ACKNOWLEDGMENTS

Funded by the Deutsche Forschungsgemeinschaft (DFG, German Research Foundation) – TRR 173 – 268565370 (projects A03, A08 and B03).

- 
- [1] T. Jungwirth, X. Marti, P. Wadley, and J. Wunderlich, Antiferromagnetic spintronics, *Nature Nanotechnology* **11**, 231 (2016).
  - [2] P. Wadley, B. Howells, J. Železný, C. Andrews, V. Hills, R. P. Campion, V. Novák, K. Olejník, F. Maccherozzi, S. S. Dhesi, S. Y. Martin, T. Wagner, J. Wunderlich, F. Freimuth, Y. Mokrousov, J. Kuneš, J. S. Chauhan, M. J. Grzybowski, A. W. Rushforth, K. W. Edmonds, B. L. Gallagher, and T. Jungwirth, Electrical switching of an antiferromagnet, *Science* **351**, 587 (2016), <https://www.science.org/doi/pdf/10.1126/science.aab1031>.
  - [3] L. Šmejkal, Y. Mokrousov, B. Yan, and A. H. MacDonald, Topological antiferromagnetic spintronics, *Nature Physics* **14**, 242 (2018).
  - [4] P. Němec, M. Fiebig, T. Kampfrath, and A. V. Kimel, Antiferromagnetic opto-spintronics, *Nature Physics* **14**, 229 (2018).
  - [5] V. Baltz, A. Manchon, M. Tsoi, T. Moriyama, T. Ono, and Y. Tserkovnyak, Antiferromagnetic spintronics, *Rev. Mod. Phys.* **90**, 015005 (2018).
  - [6] E. Rongione, O. Gueckstock, M. Mattern, O. Gomonay, H. Meer, C. Schmitt, R. Ramos, T. Kikkawa, M. Mićica, E. Saitoh, J. Sinova, H. Jaffrès, J. Mangeney, S. T. B. Goennenwein, S. Geprägs, T. Kampfrath, M. Kläui, M. Bargheer, T. S. Seifert, S. Dhillon, and R. Lebrun, Emission of coherent THz magnons in an antiferromagnetic insulator triggered by ultrafast spin-phonon interactions, *Nat Commun* **14**, 1818 (2023).
  - [7] S. Wust, C. Seibel, H. Meer, P. Herrgen, C. Schmitt, L. Baldrati, R. Ramos, T. Kikkawa, E. Saitoh, O. Gomonay, J. Sinova, Y. Mokrousov, H. C. Schneider, M. Kläui, B. Rethfeld, B. Stadtmüller, and M. Aeschliemann, Indirect optical manipulation of the antiferromagnetic order of insulating NiO by ultrafast interfacial energy transfer (2022), <https://arxiv.org/abs/2205.02686>.
  - [8] A. Ono and S. Ishihara, Ultrafast reorientation of the Néel vector in antiferromagnetic Dirac semimetals, *npj Comput. Mater.* **7**, 171 (2021).
  - [9] L. Šmejkal, T. Jungwirth, and J. Sinova, Route towards Dirac and Weyl antiferromagnetic spintronics, *physica*

- status solidi (RRL) – Rapid Research Letters **11**, 1700044 (2017).
- [10] Y. Yafet, g Factors and Spin-Lattice Relaxation of Conduction Electrons, *Solid State Physics* **14**, 1 (1963).
- [11] A. Baral and H. C. Schneider, Magnetic switching dynamics due to ultrafast exchange scattering: A model study, *Phys. Rev. B* **91**, 100402(R) (2015).
- [12] S. Essert and H. C. Schneider, Electron-phonon scattering dynamics in ferromagnetic metals and their influence on ultrafast demagnetization processes, *Phys. Rev. B* **84**, 224405 (2011).
- [13] B. Koopmans, G. Malinowski, F. Dalla Longa, D. Steiauf, M. Fähnle, T. Roth, M. Cinchetti, and M. Aeschlimann, Explaining the paradoxical diversity of ultrafast laser-induced demagnetization, *Nature Materials* **9**, 259 (2010).
- [14] M. Wu, J. Jiang, and M. Weng, Spin dynamics in semiconductors, *Physics Reports* **493**, 61 (2010).
- [15] B. Y. Mueller, A. Baral, S. Vollmar, M. Cinchetti, M. Aeschlimann, H. C. Schneider, and B. Rethfeld, Feedback effect during ultrafast demagnetization dynamics in ferromagnets, *Physical Review Letters* **111**, 167204 (2013).
- [16] M. Krauß, T. Roth, S. Alebrand, D. Steil, M. Cinchetti, M. Aeschlimann, and H. C. Schneider, Ultrafast demagnetization of ferromagnetic transition metals: The role of the coulomb interaction, *Physical Review B* **80**, 180407(R) (2009).
- [17] K. Leckron, S. Vollmar, and H. C. Schneider, Ultrafast spin-lattice relaxation in ferromagnets including spin-orbit fields, *Phys. Rev. B* **96**, 140408(R) (2017).
- [18] B. Y. Mueller and B. Rethfeld, Relaxation dynamics in laser-excited metals under nonequilibrium conditions, *Phys. Rev. B* **87**, 035139 (2013).
- [19] F. Caruso, Nonequilibrium lattice dynamics in monolayer MoS<sub>2</sub>, *The Journal of Physical Chemistry Letters* **12**, 1734 (2021).
- [20] L. Šmejkal, J. Železný, J. Sinova, and T. Jungwirth, Electric control of dirac quasiparticles by spin-orbit torque in an antiferromagnet, *Phys. Rev. Lett.* **118**, 106402 (2017).
- [21] J. Fabian and S. Das Sarma, Spin relaxation of conduction electrons in polyvalent metals: Theory and a realistic calculation, *Phys. Rev. Lett.* **81**, 5624 (1998).
- [22] F. Pientka, M. Gradhand, D. V. Fedorov, I. Mertig, and B. L. Györfy, Gauge freedom for degenerate bloch states, *Phys. Rev. B* **86**, 054413 (2012).
- [23] A. Baral, S. Vollmar, S. Kaltenborn, and H. C. Schneider, Re-examination of the elliott–yafet spin-relaxation mechanism, *New Journal of Physics* **18**, 023012 (2016).
- [24] K. Carva, M. Battiato, and P. M. Oppeneer, Ab initio investigation of the elliott–yafet electron-phonon mechanism in laser-induced ultrafast demagnetization, *Phys. Rev. Lett.* **107**, 207201 (2011).
- [25] The outliers for  $t = 17$  fs and  $t = 80$  fs are numerical artifacts resulting from the finite  $\mathbf{k}$ -grid.